Supporting Information for "Variable physical drivers of near-surface turbulence in a regulated river"

S. Guseva[1], M. Aurela[2], A. Cortés[3], R. Kivi[4], E. Lotsari[5,6], S. MacIntyre[3], I. Mammarella[7], A. Ojala[8,9,10], V. Stepanenko[11,12], P. Uotila[7], A. Vähä[7], T. Vesala[7,9], M. B. Wallin[13,14]and A. Lorke[1]

[1]Institute for Environmental Sciences, University of Koblenz-Landau, Landau, Germany

[2]Climate Research Programme, Finnish Meteorological Institute, Helsinki, Finland

[3]Earth Research Institute, University of California, Santa Barbara, California

[4]Space and Earth Observation Centre, Finnish Meteorological Institute, Sodankylä, Finland

[5]Department of Geographical and Historical Studies, University of Eastern Finland, Joensuu, Finland

[6]Department of Geography and Geology, University of Turku, Turku, Finland

[7]Institute of Atmospheric and Earth System Research (INAR)/ Physics, University of Helsinki, Helsinki, Finland

[8]Ecosystems and Environment Research Programme, Faculty of Biological and Environmental Sciences, University of Helsinki, Helsinki, Finland

[9]Institute for Atmosphere and Earth System Research/Forest Sciences, Faculty of Agriculture and Forestry, University of Helsinki, Helsinki, Finland

[10]Helsinki Institute of Sustainability Science (HELSUS), Faculty of Biological and Environmental Sciences University of Helsinki, Helsinki, Finland

[11]Laboratory for Supercomputer Modeling of Climate System Processes, Research Computing Center, Lomonosov Moscow State University, Moscow, Russia

[12]Department of Meteorology and Climatology, Faculty of Geography, Lomonosov Moscow State University, Moscow, Russia

[13]Department of Earth Sciences: Air, Water and Landscape, Uppsala University, Uppsala, Sweden

[14]Department of Aquatic Sciences and Assessment, Swedish University of Agricultural Sciences, Uppsala, Sweden

May 12, 2020, 8:51am

Contents of this file

1. Text S1 to S5
2. Figures S1 to S14
3. Tables S1 to S2

Introduction

In SI we add necessary figures and sections which are not included to the main text. Texts S1-S3 and Figures S1-S3 include the details of computation of the near-surface dissipation rate for two instruments: Acoustic Doppler Velocimeter (ADV) and Acoustic Doppler Current Profiler (ADCP). Text S4 provides the main equations for the one-dimensional $k - \varepsilon$ model used for computation of flow characteristics and turbulence. Text S5 and Figure S7 introduces the procedure of the logarithmic bin-averaging of the data scatter. Figure S4-S6 include additional time series of air and water temperature, relative humidity, water level fluctuation and significant wave height. Figure S8 explores the influence of the surface waves on the near-surface dissipation rate (see additional information in Appendix A). Figure S9, Tables S1-S2 provide detailed information about the overall performance of the bottom boundary layer scaling using the ADCP measurements. Figures S10-S11 explore the possible influence of the stratification and wind direction on the different approaches used for computation of the near-surface dissipation rate. Figures S12-S14 provide additional information of the one-dimensional $k - \varepsilon$ model performance: comparison with different approaches for estimation of the near-surface turbulence, modeling the temperature and flow velocity profiles. We believe this supplementary will provide a complete view of our manuscript.

Text S1. Optimization procedure for identification of the low frequency of the inertial subrange for ADV

The lower frequency limit ω_{low} (or we use k_{low} in the space domain in this case) of the spectral range for inertial subrange (IS) was found by solving the following optimization problem:

$$k_{low} = \arg\min_{\widetilde{k}\in\mathbb{R}} ||E_{33}(k) - \varepsilon_{fit}^{2/3}(\widetilde{k})E_{fit}(k,\widetilde{k})||, \tag{1}$$

where

$$E_{fit}(k,\widetilde{k}) = \begin{cases} const = \widetilde{k}^{-5/3}A_3\alpha_K, & \text{if } k < \widetilde{k}, \\ slope(-5/3) = k^{-5/3}A_3\alpha_K, & \text{if } k \geqslant \widetilde{k}, \end{cases} \tag{2}$$

and

$$\varepsilon_{fit}(\widetilde{k}) = \left(10^{\left\langle \log_{10}(E_{33}(k)/E_{fit}(k,\widetilde{k}))\right\rangle}\right)^{3/2}. \tag{3}$$

Here, $\varepsilon_{fit}^{2/3}(\widetilde{k})E_{fit}(k,\widetilde{k})$ is a fit consisting of an initial constant part and a -5/3 slope. The transition between the parts is defined by the breakpoint $\widetilde{k}$. The cost function $E_{33}(k) - \varepsilon_{fit}^{2/3}(\widetilde{k})E_{fit}(k,\widetilde{k})$ depends smoothly on $\widetilde{k}$ and measures the difference between the fit and the spectrum E_{33}. By minimizing the cost function, we obtain on optimal breakpoint k which defines the lower boundary of the IS. The optimization problem (1–3) is a general nonlinear optimization problem, and we solve it using the Matlab gradient-based optimization solver $fmincon$ (Figure S1). Here, the angled brackets denote averaging over all wave numbers k for which the inertial subrange fit was applied.

Text S2. Identification of the lower and upper frequencies of the inertial subrange for ADCP

The lower frequency limit for inertial subrange fitting (see Eq. 1 in the main text) was defined empirically by considering different flow and wind speed conditions (low, medium, high). We assumed the largest size of eddies l, which corresponds to the lower frequency limit of the inertial subrange, scales with the distance from the surface. It turned out that the eddy size varied between $l = 4$ – 4.5 m in the absence of a wave peak (we calculated $\omega_{low} = 2\pi\overline{u}_{flow}/l$, or depending on mean flow speed $\omega_{low} \sim 0.002$ - 0.3 rad s^{-1}). In the presence of waves, it varied between 3 – 4.5 m. The upper frequency limit for inertial

subrange fitting (ω_{low}) was defined empirically for all cases mentioned above in situations where there are no waves. In the presence of surface waves, it was defined as a frequency where function $f = S \cdot \omega$ had a minimum value on the interval $0.1 \leqslant \omega_{up} \leqslant 0.3$ rad s^{-1} for the situations when the flow velocity was low ($\overline{u}_{flow} \leqslant 0.1$ m s^{-1}) and on the interval $0.3 \leqslant \omega_{up} \leqslant 1$ rad s^{-1} in all the left cases.

Text S3. Comparison of dissipation rates from ADV and ADCP

We compare the dissipation rates estimated from single-point velocity measurements near the water surface (ADV, 0.4 m water depth) with those estimated from a bottom-mounted profiler (ADCP for the same depth (Figure S3). There was general agreement between both dissipation rates, however, there was a large scatter among individual measurements (10 min resolution) and partially also a systematic bias at high dissipation rates ($> 10^{-6}$ W kg^{-1}). The bias can be removed by applying optional quality assurance (QA) criterion (length of the observed inertial subrange, Figure S3b, c, d). While mainly high dissipation rates were removed by sharpening the QA criteria, the number of valid data points was strongly reduced (e.g. from number of data points $n = 4425$ for the data without QA to $n = 469$ for data with all QA criteria applied, Figure S3d).

Text S4. The equations of the one-dimensional $k - \varepsilon$ model

$$\frac{\partial \overline{u}}{\partial t} = -g\overline{\frac{\partial h_s}{\partial x}} + \frac{\partial}{\partial z}\left((\nu_m + \nu_t)\frac{\partial \overline{u}}{\partial z}\right), \tag{4}$$

$$\frac{\partial \overline{v}}{\partial t} = \frac{\partial}{\partial z}\left((\nu_m + \nu_t)\frac{\partial \overline{v}}{\partial z}\right), \tag{5}$$

$$\frac{\partial \overline{T}}{\partial t} = \frac{\partial}{\partial z}\left((k_m + k_t)\frac{\partial \overline{T}}{\partial z}\right) - \frac{\partial \overline{S}}{\partial z}, \tag{6}$$

where $\overline{(...)}$ stands for horizontal averaging, u, v are longitudinal and transversal velocity components, respectively, T is water temperature, ν is viscosity coefficient, k is thermal conductivity coefficient, subscripts m and t denote molecular and turbulent counterparts, h_s is free water surface height, S – kinematic radiation flux, g is the modulus of acceleration due to gravity, x is longitudinal coordinate, z – vertical coordinate directed downwards. The Coriolis force is traditionally neglected for rivers given a small width of rivers compared to barotropic Rossby radius of deformation. To close the system, equations for turbulent kinetic energy k (TKE) and its dissipation rate ε are added (Stepanenko et al., 2016).

Text S5. Logarithmic bin average of the data

Estimates of dissipation rates of turbulent kinetic energy in stationary turbulence are expected to be log-normally distributed (Baker & Gibson, 1987). For the comparison of dissipation rate estimates from measurements and predictions, we calculated bin-averages using the following procedure:

Data $\longrightarrow$ Log$_{10}$ transformation of the data $\longrightarrow$ Data rotation by α =-45° $\longrightarrow$Data splitting into bins along the 1:1 line (which coincides with the x-axis) $\longrightarrow$ Data averaging in each bin $\longrightarrow$ Data rotation by α =45° $\longrightarrow$ Reversing the logarithmic transformation

The procedure is illustrated in Figure S7. Data rotation was implemented by a right matrix multiplication $D \to A \cdot D$, where A is a 2×2 rotation matrix and D is a $2 \times n$ matrix consisting of rows data$_x$ and data$_y$:

$$A = \begin{pmatrix} \cos\alpha & -\sin\alpha \\ \sin\alpha & \cos\alpha \end{pmatrix}, \quad D = \begin{pmatrix} \text{data}_x \\ \text{data}_y \end{pmatrix}. \tag{7}$$

References

Arcement, G. J., & Schneider, V. R. (1989). *Guide for selecting Manning's roughness coefficients for natural channels and flood plains.* US Government Printing Office Washington, DC.

Baker, M. A., & Gibson, C. H. (1987). Sampling Turbulence in the Stratified Ocean: Statistical Consequences of Strong Intermittency. *Journal of Physical Oceanography*, *17*(10), 1817-1836. doi: 10.1175/1520-0485(1987)017⟨1817:STITSO⟩2.0.CO;2

Chow, V. T. (1959). *Open-channel hydraulics.* McGraw-Hill Book Co.

Feddersen, F., Trowbridge, J. H., & Williams III, A. (2007). Vertical structure of dissipation in the nearshore. *Journal of Physical Oceanography*, *37*(7), 1764–1777. doi: 10.1175/JPO3098.1

Nezu, I. (1977). *Turbulent structure in open-channel flows* (PhD dissertation). Kyoto University, Japan.

Siddiqui, M. K., & Loewen, M. R. (2007). Characteristics of the wind drift layer and microscale breaking waves. *Journal of Fluid Mechanics*, *573*, 417–456. doi: 10.1017/S0022112006003892

Stepanenko, V., Mammarella, I., Ojala, A., Miettinen, H., Lykosov, V., & Vesala, T. (2016, may). LAKE 2.0: a model for temperature, methane, carbon dioxide and oxygen dynamics in lakes. *Geoscientific Model Development*, *9*(5), 1977–2006. Retrieved from `http://www.geosci-model-dev.net/9/1977/2016/` doi: 10.5194/gmd-9-1977-2016

Tominaga, A., & Sakaki, T. (2010). Evaluation of bed shear stress from velocity measurements in gravel-bed river with local non-uniformity. In A. Dittrich (Ed.), *River flow* (pp. 187–194). A.A. Balkema, Rotterdam.

Wang, B., Liao, Q., Xiao, J., & Bootsma, H. A. (2013). A free-floating PIV system: Measure-

ments of small-scale turbulence under the wind wave surface. *Journal of Atmospheric and Oceanic Technology*, *30*(7), 1494–1510. doi: 10.1175/JTECH-D-12-00092.1

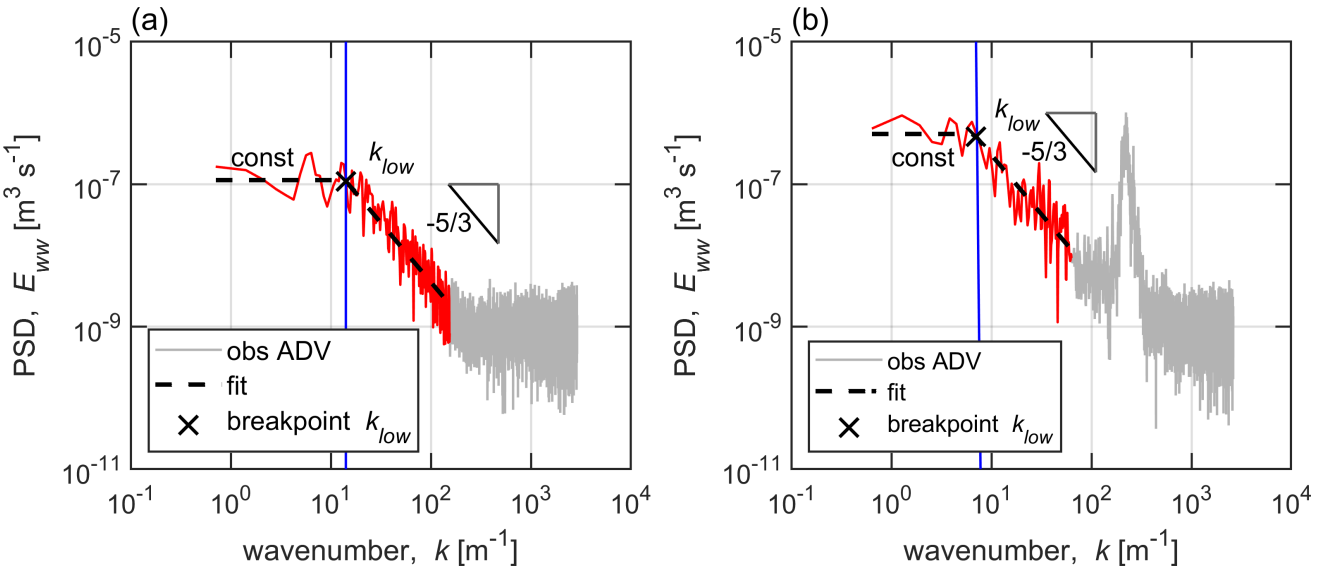

Figure S1. Typical wave number spectra (power spectral density (PSD)$E_{ww}(k)$, grey lines) of vertical velocity fluctuations observed within a 10 min period of ADV measurements: (a) without surface waves and (b) with surface waves. The part of the spectrum marked by red color was selected for spectral fitting by applying a high-frequency cut-off (see Section 2.4.1). The lower wave number limit for inertial subrange fitting (k_{low}, marked by the black cross symbol and blue vertical line) was obtained, by solving a linear optimization problem (see Text S2). The procedure seeks the breakpoint between the spectral slope equal to 1 (constant PSD) and -5/3 slope.

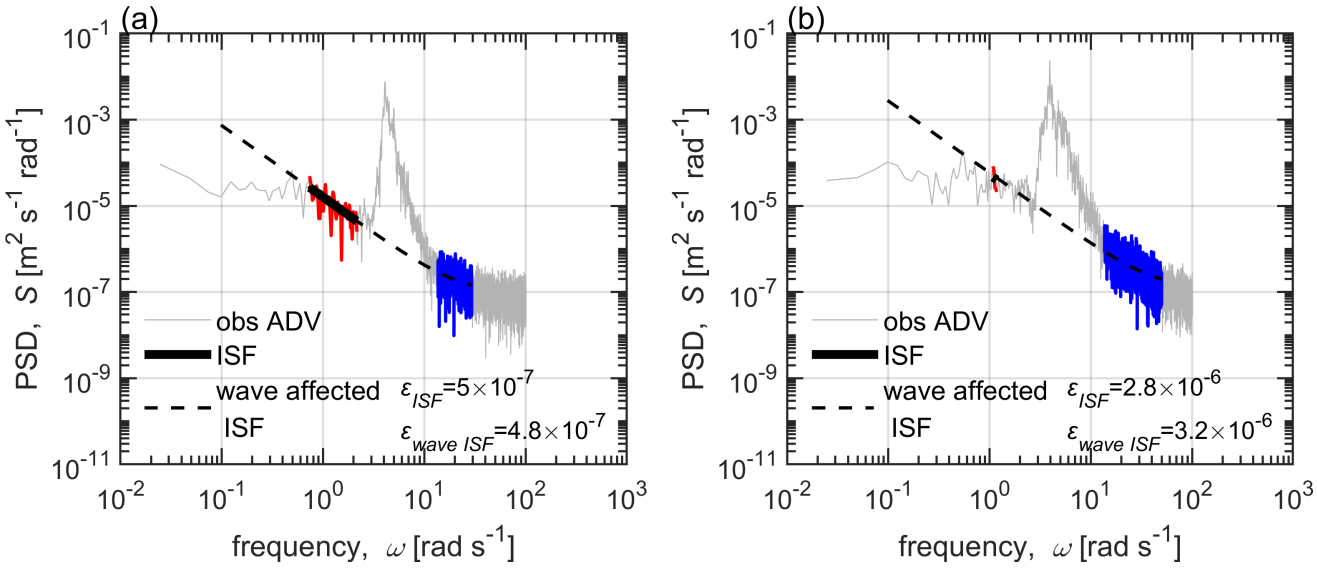

Figure S2. Typical frequency spectra (power spectral density PSD, grey lines) of vertical velocity fluctuations at 0.4 m water depth for time periods with surface waves. The frequency range marked by blue color was used for spectral fitting of the wave affected inertial subrange method (Eq. 2, see Section 2.4.1) and the range marked red for the regular inertial subrange fit (Eq. 1, see Section 2.4.1). The fit obtained from the latter is shown as a thick black line, while the extrapolated fit from the wave-affected part is shown as a black dashed line. (a) Spectrum with long inertial subrange with dissipation rate estimated from both sides of the wave peak; (b) spectrum with a short inertial subrange at frequencies before the wave peak. Whenever a sufficiently long (more than a third of the decade) inertial subrange existed to the left of the peak, we used the estimate of the dissipation rate using the regular inertial subrange fitting. Otherwise, we used the wave affected inertial subrange method. The final dissipation rate consisted of combination of both estimates.

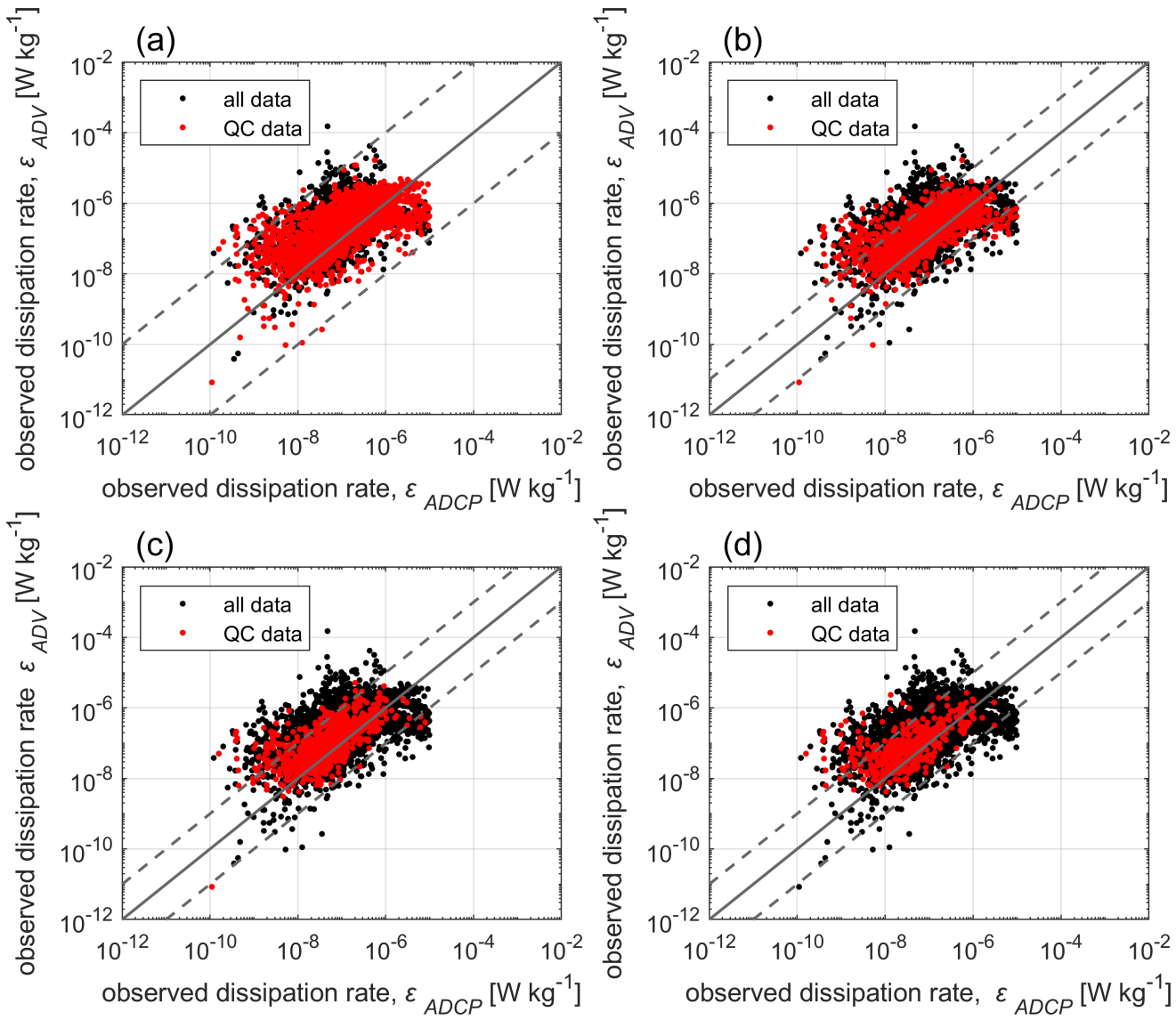

Figure S3. Observed dissipation rate from ADV ε_{ADV} at 0.4 m depth vs observed dissipation rate from ADCP ε_{ADCP} (at $\sim$ 0.4 m) obtained from inertial subrange fitting (see Eq. 1, see Section 2.4.1). For all data (black symbols) no quality check (QC) criteria were applied (number of the data points $n = 4425$). For (a) the following QC criteria were applied: criterion of frozen turbulence, coefficient of determination (red symbols, $n = 2618$), the solid grey line (also in (b)-(d)) shows a 1:1 relation between both dissipation rates and two dashed lines indicate differences of two orders of magnitude; (b) optional criterion for the length (frequency range) of the inertial subrange more than 1/5 of decade ($n = 1496$), two dashed lines indicate differences of one order of magnitude (also in (c), (d)); (c) more than 1/3 of decade ($n = 775$); (d) more than 1/2 of decade ($n = 469$).

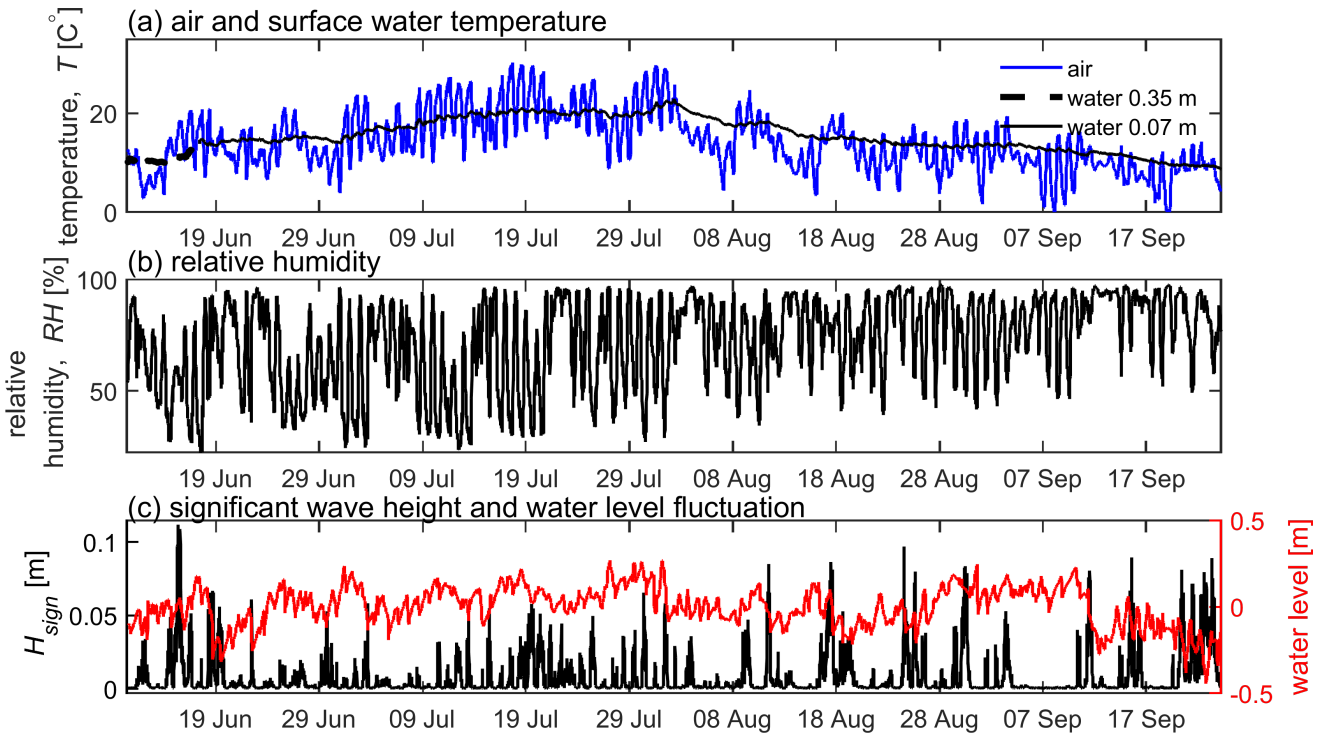

Figure S4. Time series of (a) air temperature (at 2 m height above the water, blue line) and surface water temperature (at 0.35 and 0.07 m depth, black line); (b) relative humidity. Significant wave height H_{sig} (black line) and water level fluctuations (red line). All data are shown as 10 min averages.

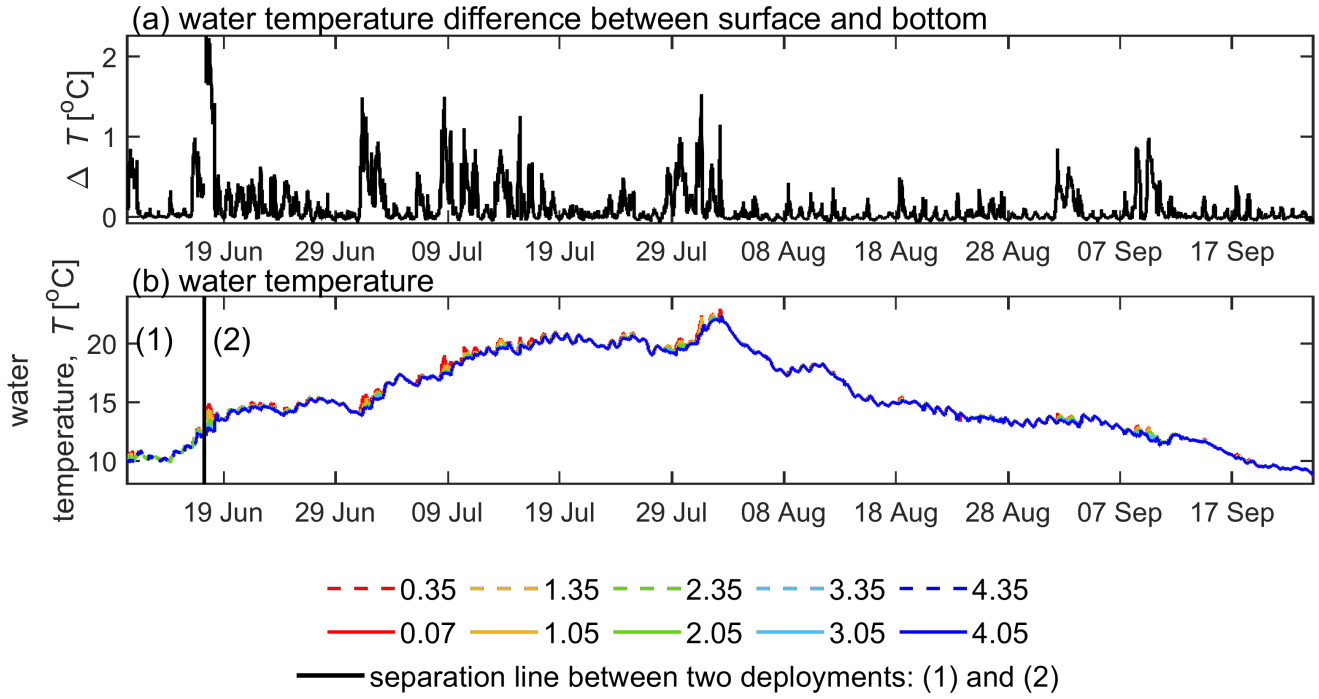

Figure S5. Time series of (a) water temperature difference between surface and bottom; (b) water temperature at different depths. The vertical black line separates two deployments periods of the thermistor chain: (1) 06.06 - 17.06 and (2) 17.06 - 24.09. All data are shown as 10 min averages.

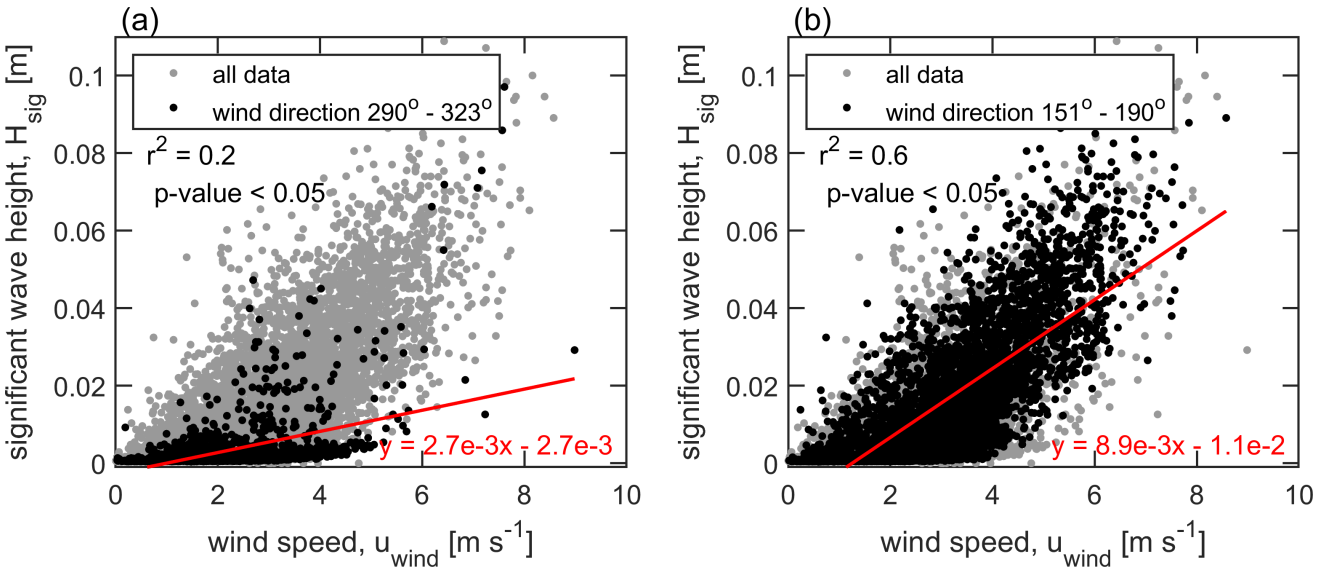

Figure S6. Significant wave height versus wind speed: (a) all data (light grey symbols) and data for which the wind direction was along aligned with the longitudinal flow velocity in the river channel ($290° \leqslant w_{dir} \leqslant 323°$, black symbols); (b) all data (grey symbols) and data for which the wind direction was against the river flow ($151° \leqslant w_{dir} \leqslant 190°$, black dots). The red lines show linear regressions (see legend), r^2 is a coefficient of determination, $p-$value is the significance level for the slope coefficient different from zero in the linear regression model.

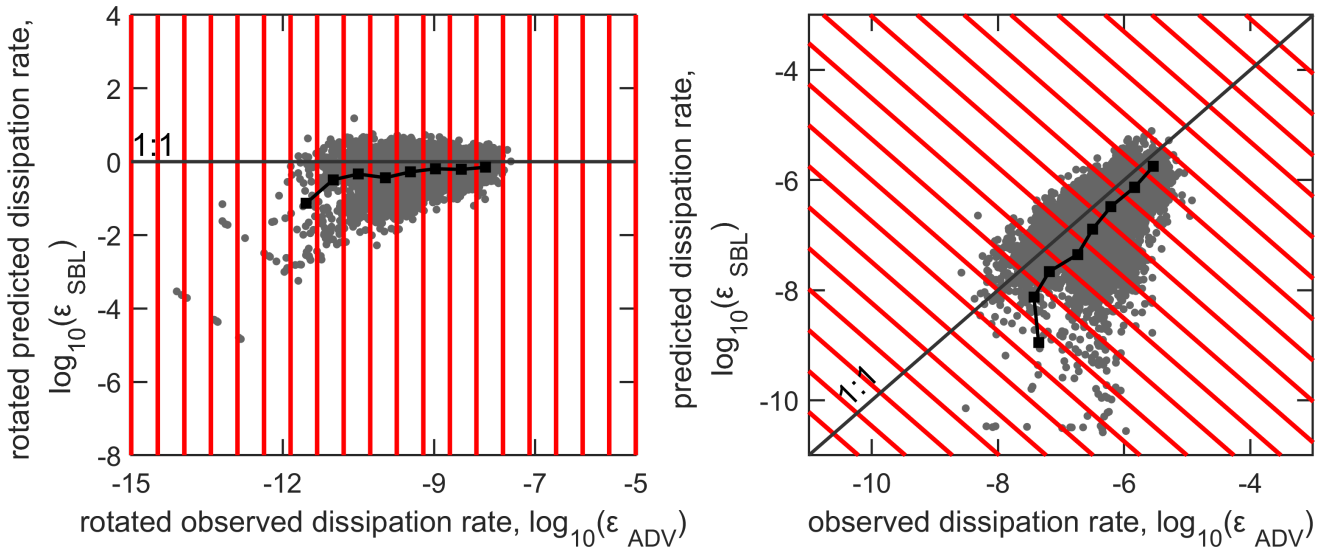

Figure S7. An example of logarithmic bin averaging of the data using measured ε_{ADV} and predicted ε_{SBL} dissipation rates from Sect. 3.2. Grey dots show: (a) rotated data (-45°); (b) original data. The solid dark grey line shows a 1:1 relationship, red lines indicate the selected intervals for averaging. The black line with square symbols shows the logarithmic bin average of the data.

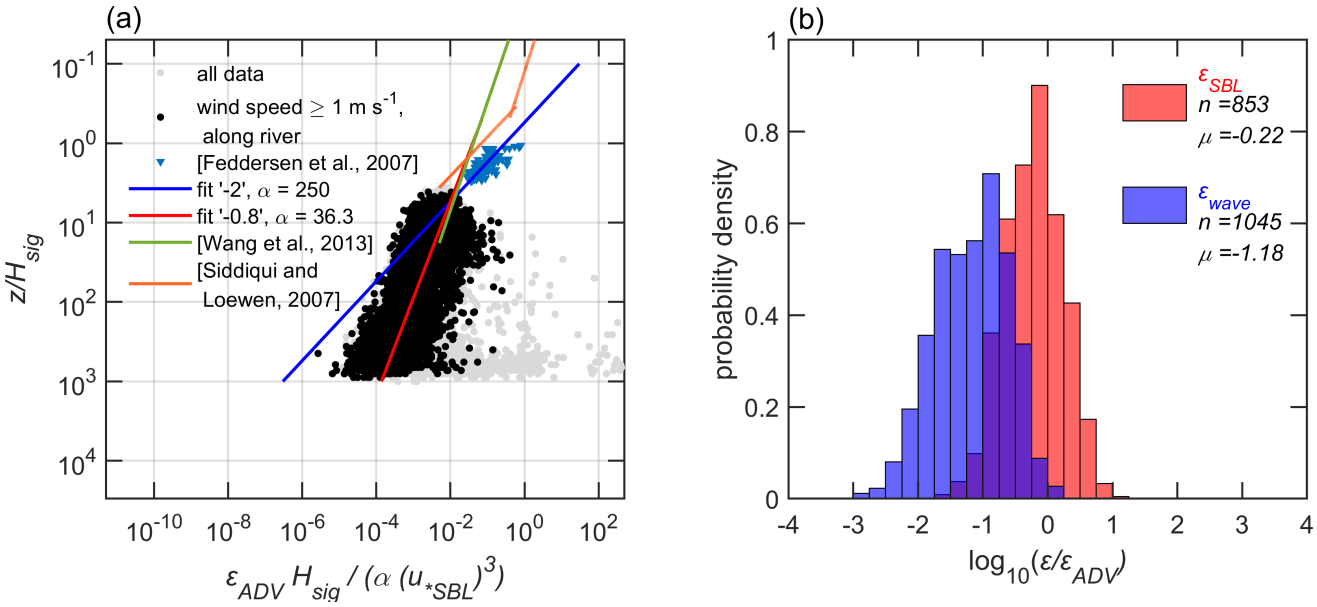

Figure S8. (a) Scaling of dissipation rate with surface waves. The x-axis shows a normalized dissipation rate (we used ε_{ADV}) and the y-axis is a wave-normalized depth (depth of the ADV measurements 0.4 m over significant wave height z/H_{sig}). Grey dots show all data, black dots highlight data for wind speed more than 1 m s^{-1} and for wind directions along the river; red line represents the fit to the data following Eq. A1 with the exponent $m = -0.8$ and the constant $\alpha = 36$ (Appendix A); blue triangles and blue line corresponds to the coastal ocean observations and its fit with the exponent $m = -2$ and the constant $\alpha = 250$ (Feddersen et al., 2007); green line represents the fit to the data obtained from a large lake with the exponent $m = -0.73$ (Wang et al., 2013); orange line shows scaling laws determined from a laboratory measurement (Siddiqui & Loewen, 2007). (b) Probability density distributions of the logarithmic ratio of predicted and observed dissipation rates. Predictions include estimates from bulk atmospheric forcing (ε_{SBL}, red color) and from wave-breaking scaling (ε_{wave}, blue color). The distributions were estimated for the selected data (black dots) in (a), but with the additional criterion of $H_{sig} > 2$ cm (empirically selected).

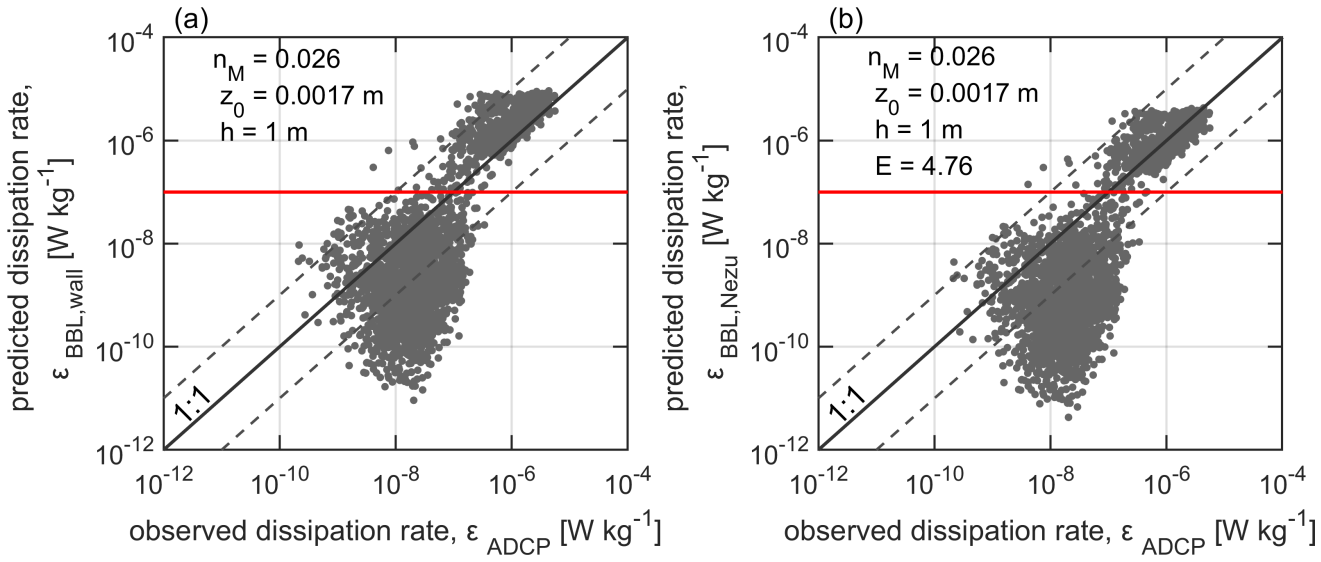

Figure S9. Bottom boundary layer scalings versus observed dissipation rate (grey points): (a) law of the wall; (b) Nezu approach. Red line shows the threshold value (10^{-7} W kg^{-1}). By assuming that the dissipation rates in the lower range were additionally affected by atmospheric forcing, we only considered dissipation rates exceeding this threshold in all subsequent analyses. n_M, z_0, h correspond to Manning's roughness coefficient, surface roughness at the sediment-water interface, the distance from the river bed, respectively. The solid grey line shows a 1:1 relation and two dashed lines indicate differences of one order of magnitude.

Table S1. Fitting parameters for the bottom boundary layer scaling (see Section 3.3). Different Manning's roughness coefficients (n_M) were used for law of the wall scaling in order to obtain the smallest error (R) between predicted $\varepsilon_{BBL,wall}$ and observed dissipation rates ε_{ADCP}. $n_M = 0.026$ s m$^{-1/3}$ corresponds to coarse sand (Chow, 1959; Arcement & Schneider, 1989). Corresponding roughness length and bottom drag coefficients are provided, the latter for a measurement height of the mean flow velocity at 1 m and at 3.8 m above the bed, respectively. 3.8 m corresponds to a water depth of 0.4 m, the sampling depth of the ADV.

Manning's roughness coefficient n_M [s m$^{-1/3}$]	Surface roughness length at the sediment-water interface z_0 [m]	Error R^a	Drag coefficient $C_{Dw,1m}$ [–]	Drag coefficient $C^b_{Dw,3.8m}$ [–]
0.026	0.0017	1.6749	0.0041	0.0028
0.0241	0.001	1.4581	0.0035	0.0025
0.023	0.00073	1.3716	0.0032	0.0023
0.0224	0.0006	1.3311	0.0031	0.0022
0.0219	0.0005	1.3011	0.0029	0.0021
0.0213	0.0004	1.2731	0.0027	0.002
0.0205	0.0003	1.2495	0.0026	0.0019
0.0195	0.0002	1.2365	0.0023	0.0017
0.0181	0.0001	1.2605	0.002	0.0015

[a] $R = 10^{\left\langle (\log_{10}\varepsilon_{wall} - \log_{10}\varepsilon_{ADCP})^2 \right\rangle}$

[b] Corresponds to 0.4 m under the water surface.

Table S2. Fitting parameters for the bottom boundary layer scaling (see Section 3.3). Selected Manning's roughness coefficient ($n_M = 0.0195$ s m$^{-1/3}$) with the least error estimate from Table S1 was used for Nezu approach. Then the empirical constant E was varied in order to obtain the smallest error between predicted $\varepsilon_{BBL,Nezu}$ and observed dissipation rates $\varepsilon_{BBL,wall}$.

Manning's roughness coefficient n_M [s m$^{-1/3}$]	Surface roughness length at the sediment-water interface z_0 [m]	Empirical constant E [–]	Error R^a
0.026	0.0017	4.76[c]	1.2394
0.0195	0.0002	4.76[c]	1.5741
0.0195	0.0002	8.43[b]	1.2528
0.0195	0.0002	9.8[c]	1.2367
0.0195	0.0002	12[c]	1.2537

[a] $R = 10^{\left\langle (\log_{10}\varepsilon_{Nezu} - \log_{10}\varepsilon_{ADCP})^2 \right\rangle}$

[b] The value was taken from (Tominaga & Sakaki, 2010).

[c] The value was taken from (Nezu, 1977).

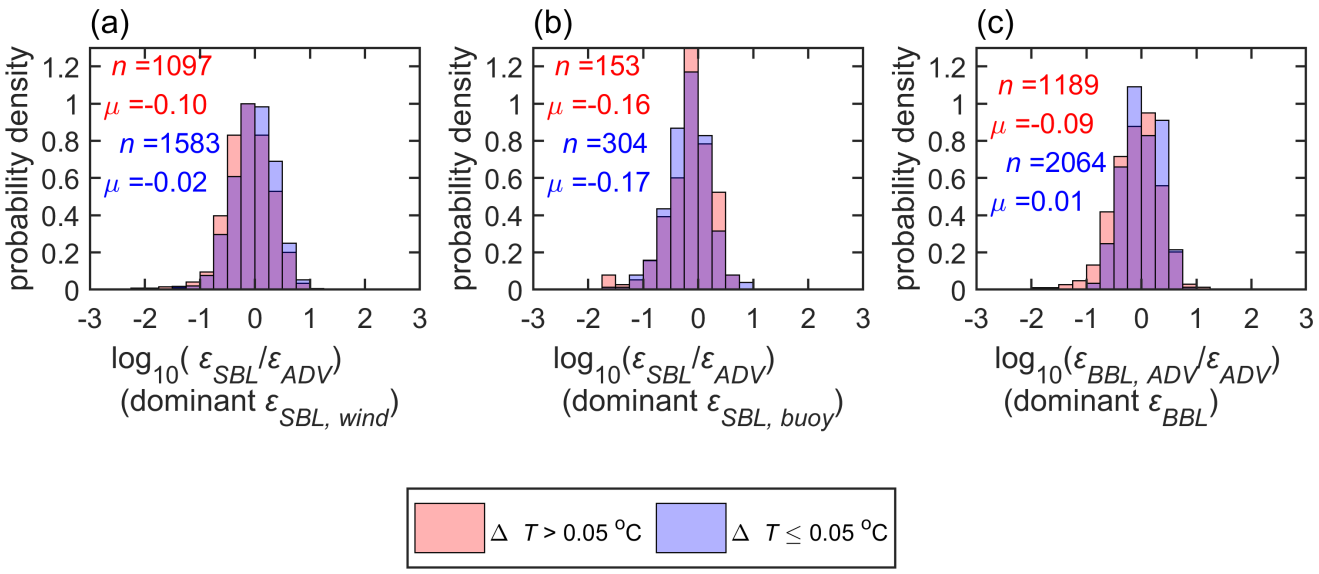

Figure S10. Probability density distributions of the ratio of predicted and observed dissipation rates when the water temperature difference between the surface and bottom (ΔT) large larger (red) or less (blue) than 0.05°C for the situations when: (a) wind; (b) buoyancy flux; (c) flow – was the dominant driver of the near-surface turbulence. The respective number of data points n and mean μ value of the logarithm of the ratio are shown the legend.

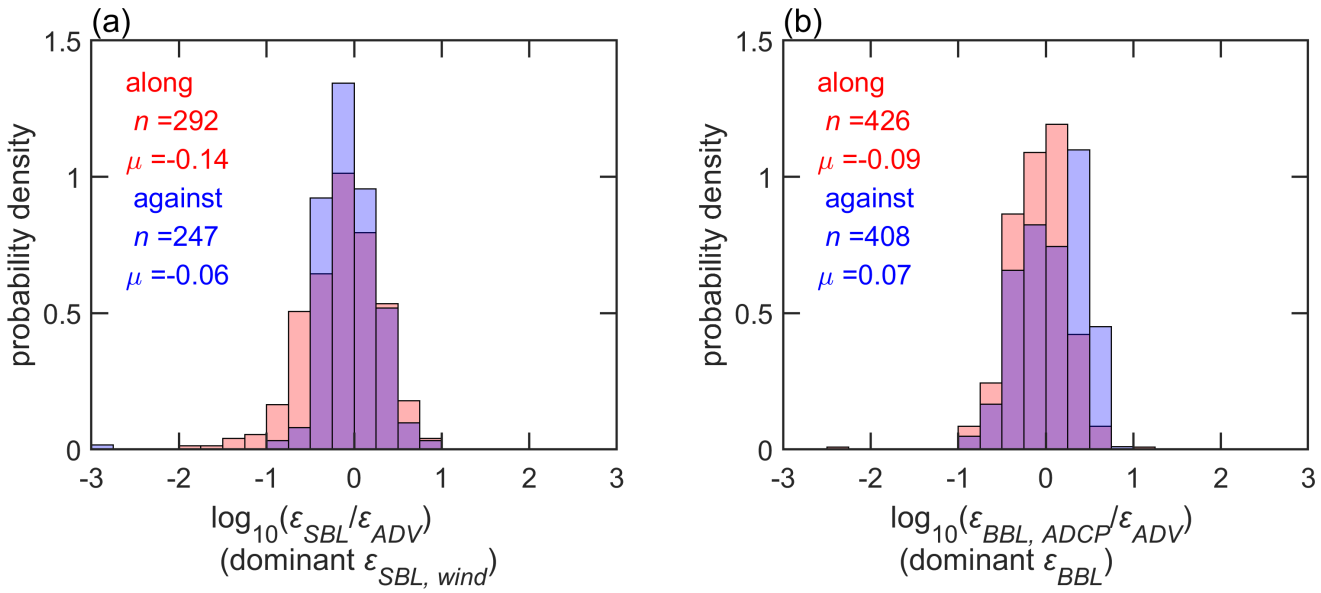

Figure S11. Probability density distributions of the ratio of predicted and observed dissipation rates for cases when wind was along the river flow ($290° \leqslant w_{dir} \leqslant 323°$, red) or against the flow ($151° \leqslant w_{dir} \leqslant 190°$, blue) for the situations when: (a) wind and (b) flow was the dominant driver of the near-surface turbulence. The respective number of data points n and mean μ value of the logarithm of the ratio are shown the legend.

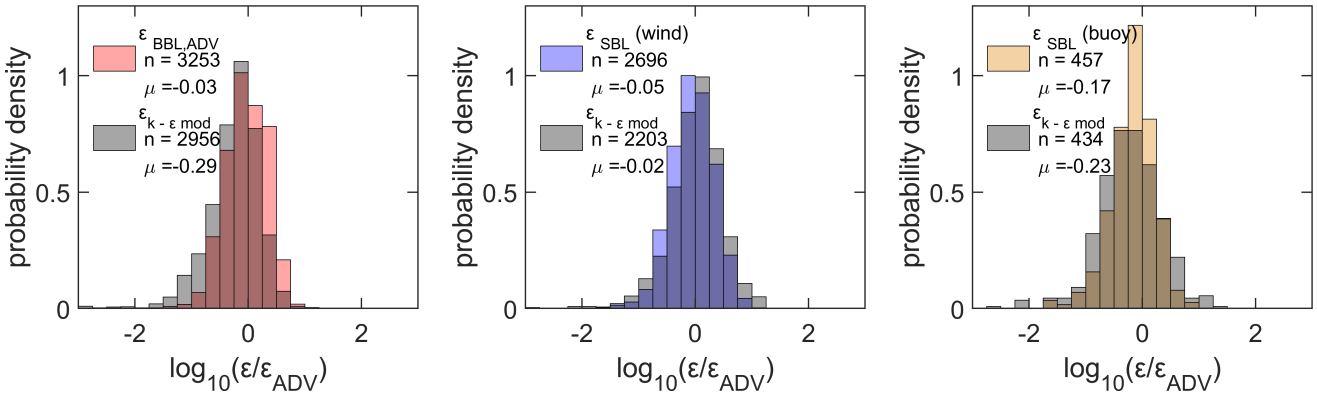

Figure S12. Probability density distributions of the logarithmic ratio of predicted and observed dissipation rates (ε_{ADV}) under different dominant forcing conditions for near-surface turbulence: (a) mean flow; (b) wind; (c) buoyancy flux. The predictions include the $k-\varepsilon$ model ($\varepsilon_{k-\varepsilon mod}$, grey color), bulk scaling using mean flow velocity ($\varepsilon_{BBL,ADV}$, red color), bulk scaling using mean wind speed (ε_{SBL}, blue color) and surface buoyancy flux (brown color). The respective number of data points n and mean μ value of the logarithm of the ratio are shown the legend.

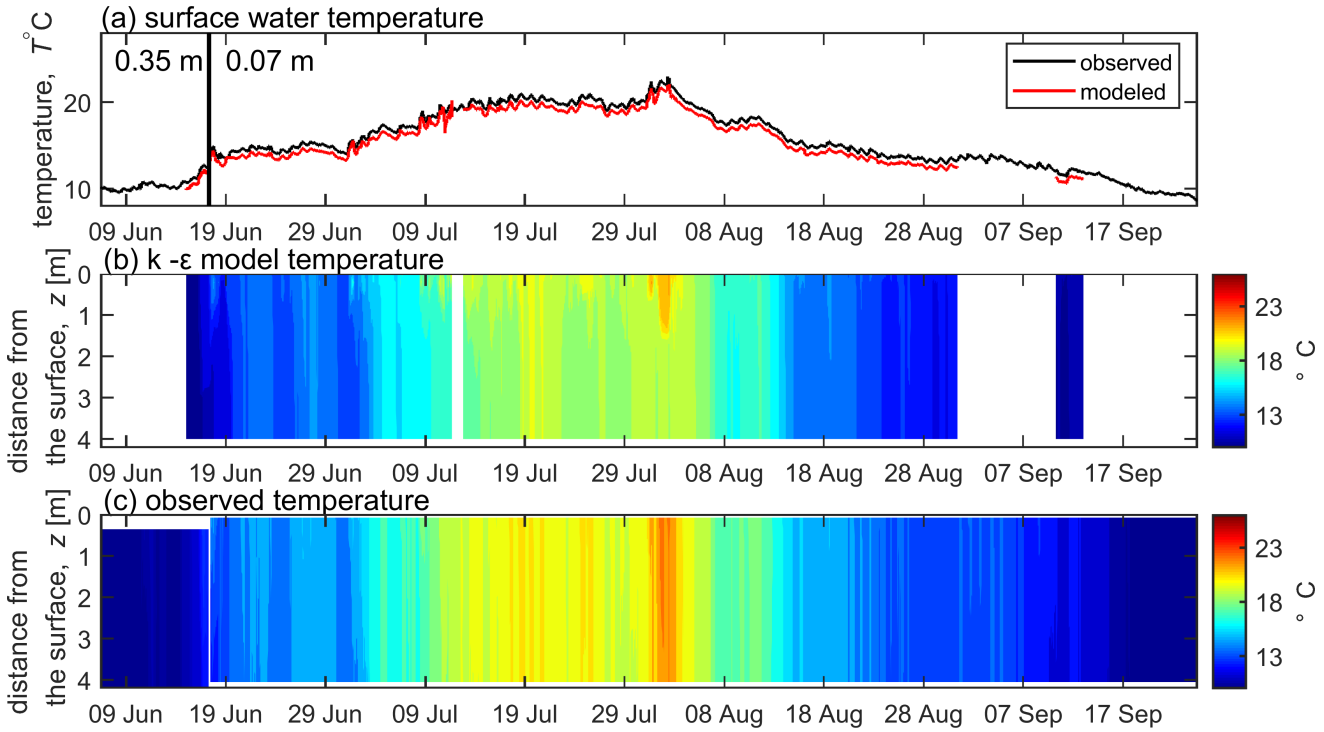

Figure S13. Time series of (a) surface water temperature: observed (black line) and modeled by $k-\varepsilon$ model (red line), vertical black line separates two deployments of the thermistor chain, numbers indicate water depth (0.35 m and 0.07 m), modeled temperature was interpolated; (b) modeled water temperature profiles; (c) observed water temperature profiles.

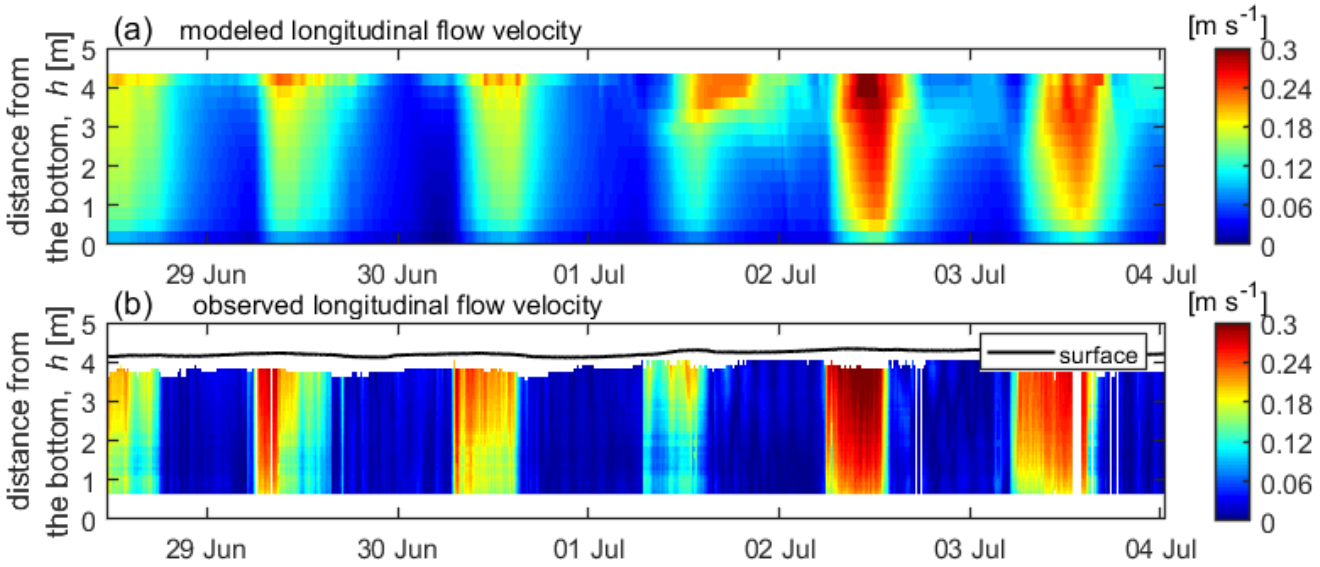

Figure S14. Time series of (a) modeled and (b) observed (ADCP) velocity profiles. Black line indicates the observed level of the water surface.